One-neutron removal from ^{29}Ne: Defining the lower limits of the island of inversion

N. Kobayashi,[1,*] T. Nakamura,[1] Y. Kondo,[1] J. A. Tostevin,[1,2] N. Aoi,[3,†] H. Baba,[3] R. Barthelemy,[4] M. A. Famiano,[4] N. Fukuda,[3] N. Inabe,[3] M. Ishihara,[3] R. Kanungo,[5] S. Kim,[6] T. Kubo,[3] G. S. Lee,[1] H. S. Lee,[6] M. Matsushita,[3,‡] T. Motobayashi,[3] T. Ohnishi,[3] N. A. Orr,[7] H. Otsu,[3] T. Sako,[1] H. Sakurai,[3] Y. Satou,[6] T. Sumikama,[8,§] H. Takeda,[3] S. Takeuchi,[3] R. Tanaka,[1] Y. Togano,[3,‖] and K. Yoneda[3]

[1]*Department of Physics, Tokyo Institute of Technology, 2-12-1 O-Okayama, Meguro, Tokyo 152-8551, Japan*
[2]*Department of Physics, Faculty of Engineering and Physical Sciences, University of Surrey, Guildford, Surrey GU2 7XH, United Kingdom*
[3]*RIKEN Nishina Center, Hirosawa 2-1, Wako, Saitama 351-0198, Japan*
[4]*Department of Physics, Western Michigan University, Kalamazoo, Michigan 49008, USA*
[5]*Astronomy and Physics Department, Saint Mary's University, Halifax, Nova Scotia B3H 3C3, Canada*
[6]*Department of Physics and Astronomy, Seoul National University, Seoul 151-742, Korea*
[7]*LPC-Caen, ENSICAEN, IN2P3-CNRS, Université de Caen, 14050 Caen Cedex, France*
[8]*Department of Physics, Tokyo University of Science, Chiba 278-8510, Japan*

(Received 6 October 2015; revised manuscript received 20 November 2015; published 20 January 2016)

Background: Very neutron-rich isotopes, including $^{30-32}$Ne, in the vicinity of $N = 20$ are known to exhibit ground states dominated by fp-shell intruder configurations: the "island of inversion." Systematics for the Ne-isotopic chain suggest that such configurations may be in strong competition with normal shell-model configurations in the ground state of ^{29}Ne.

Purpose: A determination of the structure of ^{29}Ne is thus important to delineate the extent of the island of inversion and better understand structural evolution in neutron-rich Ne isotopes. This is accomplished here through a combined investigation of nuclear and Coulomb-induced one-neutron removal reactions.

Method: Cross sections for one-neutron removal on carbon and lead targets and the parallel momentum distribution of the ^{28}Ne residues from the carbon target are measured at around 240 MeV/nucleon. The measurements are compared with reaction calculations combined with spectroscopic information from SDPF-M shell-model wave functions.

Results: The deduced width of the inclusive parallel momentum distribution, 98(12) MeV/c (FWHM), suggests that the ground state of ^{29}Ne has a spin parity of $3/2^-$. Detailed comparisons of the measured inclusive and partial cross sections of the two targets and the parallel momentum distribution of the carbon target with reaction calculations, combined with spectroscopic information from large-scale shell-model calculations, are all consistent with a $3/2^-$ spin-parity assignment.

Conclusions: The results indicate that ^{29}Ne lies within the island of inversion and that the ground state of ^{29}Ne is dominated by a $^{28}\mathrm{Ne}(0^+_1) \otimes 2p_{3/2}$ neutron configuration. Combined with recently measured interaction cross sections, it is concluded that ^{29}Ne may exhibit a moderately developed halo-like distribution.

DOI: 10.1103/PhysRevC.93.014613

I. INTRODUCTION

Understanding the evolution of shell structure in neutron-rich nuclei is a fundamental challenge for modern nuclear physics [1]. While some theoretical and experimental studies suggest the need to modify the conventional j-j-coupled shell-model (SM) basis (e.g., Ref. [2]), the mechanism driving shell evolution remains to be fully explained. In particular, the "island of inversion" region of light neutron-rich nuclei with neutron number $N \approx 20$ has been much studied [1,3]. Here the nuclei have low-lying states characterized by significant neutron fp-shell *intruder* configurations associated with deformation [4].

The work by Hamamoto [5–7] has shown that such deformation may arise due to the near-degeneracy of the $1f_{7/2}$ and $2p_{3/2}$ orbitals, which couple strongly via the spin-independent quadrupole-quadrupole interaction: an example of the Jahn-Teller effect [8,9]. Such near-degeneracy, which can be interpreted as a loss of $N = 28$ magicity, is expected to be associated with the presence of weakly bound and/or resonant neutron single-particle levels with low orbital angular momenta. As a result, weakly bound, low-ℓ neutron configurations and possible halo formation are expected to be features of island-of-inversion nuclei.

Deformation-driven halo configurations have indeed been found in the weakly bound island-of-inversion nuclei ^{31}Ne [10–12] and ^{37}Mg [13,14]. By combining one-neutron ($1n$)-removal reactions on carbon and lead targets and exploiting

*Present address: National Superconducting Cyclotron Laboratory, Michigan State University, East Lansing, Michigan 48824-1321, USA; kobayashi@nscl.msu.edu
†Present address: RCNP, Osaka University, Mihogaoka, Ibaraki, Osaka 567-0047, Japan.
‡Present address: CNS, University of Tokyo, RIKEN Campus, Wako, Saitama 351-0198, Japan.
§Present address: Department of Physics, Tohoku University, Miyagi 980-8578, Japan.
‖Present address: Department of Physics, Tokyo Institute of Technology, 2-12-1 O-Okayama, Meguro, Tokyo 152-8551, Japan.

 ©2016 American Physical Society

their different sensitivities to the configurations of the removed neutron, the ^{31}Ne ground state has been demonstrated to have spin parity $3/2^-$ [10,11]. This result, consistent with the large-scale SM calculations with the SDPF-M effective interaction [15], shows that the very weakly bound ^{31}Ne ground state [16] has a sizable $2p_{3/2}$ halo component. The SM calculations indicate that the ^{31}Ne ground state is dominated by $3p$-$2h$ configurations and is suggestive of a large prolate deformation ($\beta \approx 0.6$).

In addition to ^{31}Ne, there is now a body of experimental data on the very neutron-rich Ne isotopes [12,17–23]. The structures of these isotopes evolve considerably as one moves toward the neutron drip line and are complex. As demonstrated for the cases of ^{31}Ne and ^{37}Mg, modern large-scale SM calculations provide theoretical guidance of this evolution within the island of inversion. Specifically, multiple particle-hole components in the ground and low-lying excited states are predicted, with changes to the ground-state spin parities from those expected based on the normal ordering and filling of nuclear single-particle orbitals.

For the lighter neutron-rich neon isotopes, neutron removal from ^{28}Ne suggested that significant $2p_{3/2}$ intruder configurations are present at low excitation energies in ^{27}Ne [18]. Recent ^{26}Ne(d, p) reaction studies have demonstrated that the lowest $3/2^-$ state is at 765 keV, while the ^{27}Ne ground state is $3/2^+$ [18–21] (see also Fig. 4 in Sec. IV A). This observed level ordering is in agreement with the SDPF-M SM level scheme, which, however, places the lowest ^{27}Ne($3/2^-$) state at 170 keV in excitation. In contrast, the SM calculations predict the lowest ^{31}Ne($3/2^+$) state to be at 680 keV. This excited $3/2^+$ level has not yet been observed experimentally.

Hence, both experimentally and according to the SDPF-M, there is a spin-parity inversion of the ground states between ^{27}Ne and ^{31}Ne. For ^{29}Ne, of interest here, the ground-state spin parity has not been reported. The SDPF-M SM prediction is that the $3/2^+$ and $3/2^-$ states are essentially degenerate, with the $3/2^-$ state lying only 73 keV above the $3/2^+$ ground state. These predictions are of particular interest as, based on mass measurements, ^{29}Ne has long been thought to lie outside the island of inversion [24,25]. Other data of relevance are the interaction cross-section measurements by Takechi *et al.* [12], which show a difference in the cross sections for ^{29}Ne and ^{28}Ne comparable to that between ^{31}Ne and ^{30}Ne, suggestive of low-ℓ valence neutron ground-state configurations. Similarly, the inclusive momentum distribution in neutron removal from ^{30}Ne has been reported to be relatively narrow (136(2) MeV/c [22]), indicative of large $p_{3/2}$ and/or $s_{1/2}$ and small $d_{3/2}$ removal strengths to bound ^{29}Ne final states. Finally, the β-decay data on ^{29}Ne [23] were analyzed assuming a $3/2^+$ ^{29}Ne ground state but placing no significant constraint upon this spin assignment.

Here we discuss data for the $1n$-removal reactions from ^{29}Ne on carbon and lead targets and compare these with the theoretical expectations from SDPF-M SM wave functions (and spectroscopic strengths of their $1n$ overlaps) for ^{29}Ne(J^π) and ^{28}Ne. We deduce the shell structure of the ^{29}Ne ground state (^{29}Ne$_{\rm g.s.}$) by exploiting the distinct sensitivities of the nuclear- and Coulomb-dominated $1n$-removal reaction mechanisms on the two targets to the single-particle wave functions of the active valence neutrons [26–28].

The present experiment was carried out at a beam energy of around 240 MeV/nucleon. We show, as demonstrated in the recent work on ^{31}Ne [11], that a combined analysis of the cross sections for the two reactions, and of the momentum distribution of the reaction residues on the carbon target, allows one to deduce the J^π and the spectroscopic factor, C^2S, of the assumed theoretical $\langle\, ^{28}\mathrm{Ne}(0^+_1)|^{29}\mathrm{Ne}_{\rm g.s.}(J^\pi)\rangle$ overlap. We note that for ^{29}Ne, unlike for the case of ^{31}Ne, the neutron separation energy S_n is relatively well known experimentally ($S_n = 960(140)$ keV [29,30]), allowing for a quantitative comparison of the spectroscopic factors extracted from the data for the two independent reaction mechanisms and the values predicted by the SDPF-M SM calculations.

II. EXPERIMENT

The experiment was performed at the RI Beam Factory (RIBF) [31] at RIKEN, using a ^{48}Ca primary beam at 345 MeV/nucleon, with an intensity ≈50 pnA supplied by the Superconducting Ring Cyclotron. The experimental setup is identical to that used for the earlier reported ^{37}Mg experiment [13]. Hence, only a brief overview of the experimental details is presented.

The ^{29}Ne secondary beam, produced by projectile fragmentation of ^{48}Ca on a 15-mm-thick rotating Be target, had a typical intensity of $\approx 1 \times 10^2$ particles per second and a momentum spread ($\Delta P/P$) of ±0.5%. Each ^{29}Ne particle was identified according to the magnetic rigidity ($B\rho$), time of flight, and energy loss (ΔE) obtained using the standard detectors of the fragment separator BigRIPS [32,33]. The midtarget energies for the $1n$-removal reactions were 244 MeV/nucleon for the Pb target (3.37 g/cm^2) and 240 MeV/nucleon for the C target (2.54 g/cm^2). The ^{28}Ne residues were identified by their $B\rho$, time of flight, and ΔE measured using the ZeroDegree Spectrometer (ZDS) and associated detectors [32,33]. In addition, the DALI2 NaI array [34] was installed, surrounding the reaction target, to detect γ rays emitted from those ^{28}Ne residues populated in excited states.

III. DATA ANALYSIS

We discuss first the experimental results and then their interpretation using comparisons with SM predictions for the possible ^{29}Ne ground-state configurations and their corresponding $1n$ overlaps with the final states of ^{28}Ne. This section discusses the experimental results.

A. Cross sections

The measured cross sections for the two targets and the deduced Coulomb contribution to the cross section for the lead target are listed in Table I. The third row of data in Table I shows the inclusive $1n$-removal cross sections for all bound final states of ^{28}Ne from Pb [σ_{-1n}(Pb)] and C [σ_{-1n}(C)]. The contribution deduced to arise from electric dipole ($E1$) Coulomb dissociation [$\sigma_{-1n}(E1)$] is also shown

TABLE I. Measured $1n$-removal cross sections of ^{29}Ne on Pb [σ_{-1n}(Pb)] and C [σ_{-1n}(C)] targets and the deduced Coulomb breakup contribution on Pb [$\sigma_{-1n}(E1)$]]. The first three rows list the partial cross sections for direct feeding of ^{28}Ne(0_1^+), the partial cross sections for all excited states decaying via the 1293-keV γ ray, and the inclusive $1n$-removal cross sections. The percentage of the cross section that directly feeds ^{28}Ne(0_1^+) is also shown.

	σ_{-1n}(Pb) (mb)	$\sigma_{-1n}(E1)$ (mb)	σ_{-1n}(C) (mb)
Reaction			
(^{29}Ne, ^{28}Ne(0_1^+))	252(45)	176(50)	36(7)
(^{29}Ne, ^{28}Ne*)	127(43)	46(49)	38(7)
(^{29}Ne, ^{28}Ne), inclusive	379(14)	222(36)	74(2)
Ground-state fraction	66(12)%	79(26)%	49(9)%

for the Pb target. The latter is obtained by subtracting a nuclear contribution for the Pb target, estimated by scaling (by a geometrical factor Γ) the measured σ_{-1n}(C) value, i.e.,

$$\sigma_{-1n}(E1) = \sigma_{-1n}(\mathrm{Pb}) - \Gamma\sigma_{-1n}(\mathrm{C}). \quad (1)$$

The calculated $\sigma_{-1n}(E1)$ values in Table I use a factor $\Gamma = 2.13(45)$, discussed in Refs. [10,11] and [13], which includes a conservative estimate of the associated uncertainty. In Sec. IV C 1 we revisit this choice and also show the relative insensitivity of the present analysis to the details of Γ. There we use eikonal reaction model calculations of the nuclear breakup contributions to compute theoretical Γ_{th} values. We note in advance that using these Γ_{th} values or the above geometrical Γ estimate [10] does not materially affect the present (or earlier) results, given the large relative magnitudes of the $1n$-removal cross sections for the Pb and C targets—particularly for the ground-state transitions involving weakly bound neutron removal.

To examine the valence neutron configuration of ^{29}Ne quantitatively the inclusive cross section σ_{-1n} is resolved into partial cross sections feeding the ^{28}Ne(0_1^+) and bound excited states (^{28}Ne*) using γ rays measured in coincidence with the ^{28}Ne residues. Figure 1 shows these Doppler-shift-corrected γ-ray coincidence spectra for the C and Pb targets. For the C target, peaks near 936, 1293, and 1536 keV are observed. The 936- and 1293-keV peaks were observed in Ref. [35], where the latter was attributed to the $2_1^+ \rightarrow 0_1^+$ transition. The observation of the 1536(17)-keV line is new to this work. If this transition is not included in the fit, the width of the 1293-keV peak is too wide ($\sigma \approx 160$ keV) to be explained by the experimental resolution ($\sigma \approx 70$ keV).

According to the SDPF-M SM calculations, the bound ^{28}Ne excited states above the 2_1^+ state decay essentially exclusively via the 2_1^+ state (>99%), and their direct decays to the ground state are thus negligible. For the 1536-keV transition, this is supported by the observation of a 1536-keV peak when gating the γ-γ coincidence data set on the 1293-keV peak, as shown in the inset in Fig. 1(a). The 25(12) counts observed in this 1536-keV coincidence photopeak is consistent with the 29 counts expected from such a cascade. We find a similar consistency for the Pb target data set.

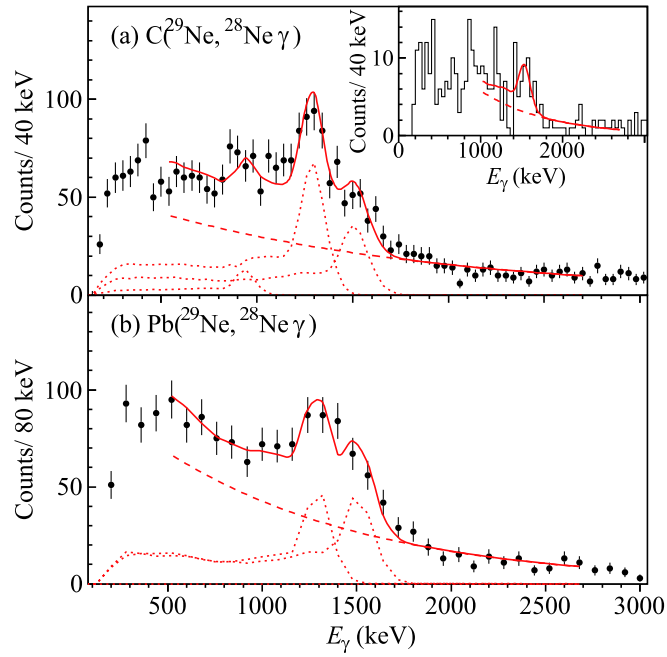

FIG. 1. Measured γ-ray energy spectra in coincidence with ^{28}Ne residues following $1n$ removal from ^{29}Ne on C (a) and Pb (b) targets. Solid (red) lines show the fits to the spectra based on the simulated detector response functions [dotted (red) lines] and exponential backgrounds [dashed (red) lines]. The inset in (a) is discussed in the text.

The partial cross sections to the excited states of ^{28}Ne for the C target are obtained by a fit to the γ-ray spectrum with response functions, obtained from a Geant4 simulation, plus an assumed exponentially decreasing background, as shown in Fig. 1(a). For the Pb target [Fig. 1(b)], the 936-, 1293-, and 1536-keV transitions are included in the fit to the γ-ray spectrum, however, we find that the intensity of the 936-keV peak is consistent with 0. Table I also lists the deduced partial cross sections for direct feeding of ^{28}Ne(0_1^+) for the C and Pb targets, denoted $\sigma_{-1n}(\mathrm{C}; 0_1^+)$ and $\sigma_{-1n}(\mathrm{Pb}; 0_1^+)$, obtained by subtracting the values for the $2_1^+ \rightarrow 0_1^+$ transition, in the second row of data, from the inclusive cross sections. The stated Coulomb breakup partial cross section feeding the ^{28}Ne(0_1^+), $\sigma_{-1n}(E1; 0_1^+)$, is obtained from

$$\sigma_{-1n}(E1; 0_1^+) = \sigma_{-1n}(\mathrm{Pb}; 0_1^+) - \Gamma\sigma_{-1n}(\mathrm{C}; 0_1^+). \quad (2)$$

B. Momentum distribution of ^{28}Ne residues

The inclusive momentum distribution of the ^{28}Ne residues, in the ^{29}Ne rest frame, following $1n$ removal on the C target is shown in Fig. 2. The laboratory frame momenta of the ^{28}Ne were extracted using the time of flight and the difference in the flight lengths of the trajectories. To translate these to the ^{29}Ne rest frame, we also extract the momentum of the incoming ^{29}Ne projectile, determined in the same manner as for the ^{28}Ne residues. For realistic perpendicular momentum components, of a few hundreds of MeV/c, the measured ^{28}Ne residue momenta and their parallel components agree to a high precision. Hereafter, we present cross section distributions

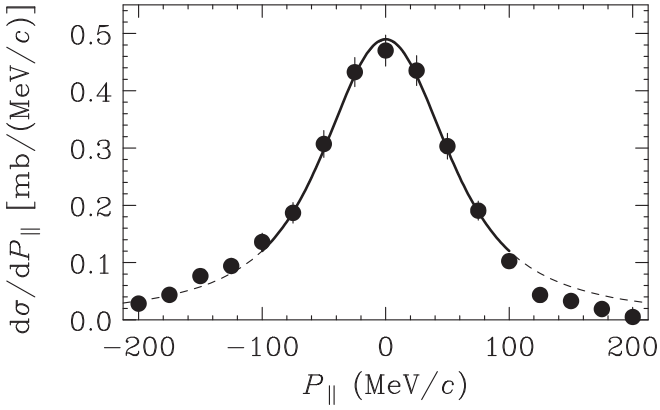

FIG. 2. Measured ^{28}Ne inclusive longitudinal momentum distribution following neutron removal reactions on the carbon target. The solid line is a fit to the data, for momenta between ± 100 MeV/c, using a Lorentzian function convoluted with a Gaussian experimental resolution with $\sigma = 22$ MeV/c.

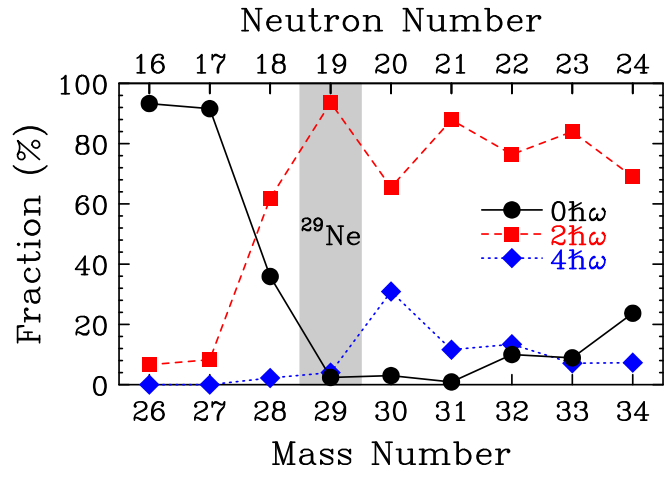

FIG. 3. Fractions of the $0\hbar\omega$ (black circles), $2\hbar\omega$ [(red) squares], and $4\hbar\omega$ [(blue) diamonds] configurations in the ground states of the Ne isotopes, as given by the SDPF-M [15] SM calculations. For ^{29}Ne, the calculation is for the $3/2^+$ SM ground state. For the $3/2^-$ state, which is found here to be the ^{29}Ne ground state, the $(1+3)\hbar\omega$ configuration is dominant (Sec. V).

referred to these parallel components. The width of the distribution is deduced to be 98(12) MeV/c (FWHM) based on a fit using a Lorentzian lineshape convoluted with a Gaussian experimental resolution with $\sigma = 22$ MeV/c. Such a relatively narrow momentum distribution is indicative of significant low-ℓ components in the valence neutron wave function in ^{29}Ne, consistent with the conjecture in Ref. [12] based on the ^{29}Ne interaction cross section.

IV. THEORETICAL INTERPRETATION

In the following, we present the results of calculations of the cross sections and momentum distributions of the reaction residues for the dominant neutron-removal reaction mechanisms on the C and Pb targets. These are combined with the results of large-scale SM calculations to enable detailed comparisons of the experimental data with the theoretical expectations for further investigation of the ground-state configuration of ^{29}Ne.

A. Shell-model calculations

The SDPF-M effective interaction is used for SM calculations in the present study. The calculations allow an arbitrary number of neutron excitations across the $N = 20$ shell gap. The results for the ground-state wave functions of the neutron-rich Ne isotopes, and for the low-energy spectra of states of the odd-N ^{27,29,31}Ne isotopes, are summarized in Figs. 3 and 4, respectively. Figure 3 shows the changes in the percentages of $n\hbar\omega$ components in the ground states with N, showing the rapid change in the ground-state configurations between $N = 17$ and $N = 19$: from a dominantly $0\hbar\omega$ to a dominantly $2\hbar\omega$ configuration. Figure 4 shows the energy spectra of ^{27,29,31}Ne. In the ^{29}Ne case, we note the near-degeneracy of the lowest $3/2^+$ and $3/2^-$ states from the SM calculations and that low-energy states with spin parities $3/2^+, 3/2^-, 7/2^-$, and $1/2^+$ are predicted. In the case of the negative-parity states, $1\hbar\omega$ and $3\hbar\omega$ configurations dominate the wave functions (Sec. V). Interestingly, a similar competition between the positive- and the negative-parity intruder levels was predicted for ^{29}Ne in the original SM study of the island of inversion by Warburton, Becker and Brown [4].

The experimentally known levels of ^{29}Ne shown in Fig. 4 were observed in a recent in-beam γ-ray spectroscopic study [22], although spin-parity assignments were not made. In the case of the excited states of ^{27}Ne, the SDPF-M interaction has some difficulty predicting the energy of the $7/2^-$ level, found near 2 MeV in a recent ^{26}Ne(d, p) reaction study [21].

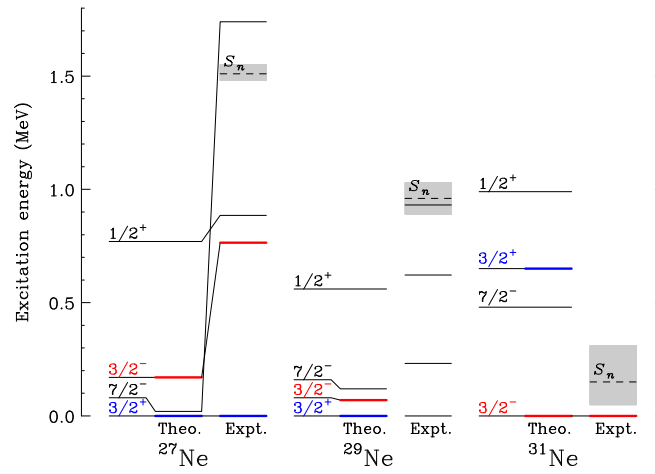

FIG. 4. Low-lying shell-model states of ^{27,29,31}Ne with spin parities $3/2^+$, $3/2^-$, $7/2^-$, and $1/2^+$ calculated with the SDPF-M interaction. The relative positions of the $3/2^+$ and $3/2^-$ states are highlighted. The experimental energy level scheme of ^{27}Ne is based on Refs. [18–21]. For ^{29}Ne, the experimental level scheme is based on Ref. [22]. For ^{31}Ne, the ground-state spin parity of $3/2^-$ and separation energy of $0.15^{+0.16}_{-0.10}$ MeV were obtained from an analysis of Coulomb and nuclear breakup reactions [11]. The experimental separation energies of ^{27,29}Ne are taken from Ref. [29].

That reaction study also confirmed the $3/2^-$ assignment of the level seen experimentally at 765 keV and predicted at 170 keV. Thus, the SM calculations provide only guidance, and in the following we examine the possibility that the ^{29}Ne ground state has spin parity $3/2^+$, $3/2^-$, $7/2^-$, or $1/2^+$.

B. Carbon target analysis

1. Cross sections

In the case of the carbon target, the eikonal model theoretical description of the strong-interaction-dominated nucleon-removal reaction dynamics uses the sudden (fast-collision) and eikonal (forward-scattering) approximations. This has been presented and discussed in detail elsewhere (e.g., Refs. [26] and [36], and references therein). The model assumes that for the fast, surface-grazing interactions of the mass A projectile with the target, which dominate the single-nucleon-removal channel, the state α of the mass $A-1$ reaction residue is a spectator. Thus, the yield of residues in a particular final state α reflects the component of this configuration in the ground-state wave function of the projectile. The ratio of observed inelastic cross sections of (deformed) nuclei with $A \approx 30$ and collisions at $\approx$240 MeV/nucleon, of order 10 mb [37], to the cross section for elastic scattering of the residues, of typically 1 b, suggests that spectator-core model uncertainties of partial cross sections and momentum distributions enter at the 1% level.

The partial cross section for removal of a nucleon from a given ground-state configuration J^π and population of a residue final state α with excitation energy E^*_α, is calculated as

$$\sigma^{\rm th}_{-1n}(\alpha) = \left(\frac{A}{A-1}\right)^{N_{\rm osc}} C^2S(\alpha, J^\pi)\,\sigma_{\rm sp}(J, S^*_\alpha), \qquad (3)$$

where $S^*_\alpha = S_n + E^*_\alpha$ is the effective separation energy for the final state α and S_n is the ground state–to–ground state nucleon separation energy. Here $N_{\rm osc}$, in the A-dependent center-of-mass correction factor, which multiplies the SM spectroscopic factors $C^2S(\alpha, J^\pi)$, is the number of oscillator quanta associated with the major shell of the removed particle [38]. The single-particle cross section $\sigma_{\rm sp}$ is the sum of the elastic and inelastic breakup contributions to the reaction [36], $\sigma_{\rm sp} = \sigma^{\rm inel}_{\rm sp} + \sigma^{\rm elas}_{\rm sp}$, calculated assuming that the removed nucleon's single-particle wave function (or overlap) is normalized to 1. The theoretical inclusive nucleon-removal cross sections, $\sigma^{\rm th}_{-1n}$, are computed as the sum of these partial cross sections $\sigma^{\rm th}_{-1n}(\alpha)$ for all bound SM final states of the mass $A-1$ residue.

The reaction model inputs use the systematic approach detailed in Sec. III of Ref. [41]. The geometries of the complex optical potentials of the neutron and the residue with the ^{12}C target and of the real potentials that bind the removed neutrons are deduced from the density of ^{28}Ne and the root mean squared (rms) radii of the active neutron orbitals, respectively, both given by spherical Hartree-Fock calculations. A Gaussian ^{12}C target density with an rms radius of 2.32 fm, consistent with the measured charge radius, and a zero-range effective two-nucleon interaction were assumed. Our ^{28}Ne target S matrix calculates a reaction cross section of 1250 mb, within 2% of the measured interaction cross-section value (at 240 MeV/nucleon) of Takechi *et al.* [12]. The Woods-Saxon neutron binding potentials have a fixed diffuseness (0.7 fm) and spin-orbit strength (6 MeV). The deduced radius parameters of the potentials, r_0, were 1.250 fm for the $2s_{1/2}$, $2p_{3/2}$, and $1f_{7/2}$ neutron orbitals and 1.243 fm for the $1d_{3/2}$ and $1d_{5/2}$ orbitals. The depth of each binding potential was adjusted to reproduce the physical separation energy of the removal reaction to the final state of interest, i.e., S^*_α in Eq. (3).

TABLE II. Summary of the calculated $1n$-removal cross sections of ^{29}Ne on C ($\sigma^{\rm th}_{-1n}$) for the different assumed spin parities of ^{29}Ne$_{\rm g.s.}$, collected from Tables VI and VII. The cross section for the ^{28}Ne ground state, the summed cross sections to all bound excited states, and the fractional (percentage) contributions of the ground-state (g.s.) transition are listed. Measured values are also included.

	^{29}Ne: J^π				
	$3/2^+$	$3/2^-$	$7/2^-$	$1/2^+$	Expt.
$\sigma^{\rm th}_{-1n}$ (mb)					
^{28}Ne(0^+_1)	13.25	31.60	15.87	2.71	36(7)
^{28}Ne*	49.82	37.41	32.24	52.41	38(7)
Inclusive	63.07	69.01	48.11	55.13	74(2)
g.s. fraction	21%	46%	33%	5%	49(9)%

The cross sections have been calculated assuming the ^{29}Ne(J^π) ground state to be described by the lowest-lying SDPF-M SM wave functions with spin parities $3/2^+$, $3/2^-$, $7/2^-$, and $1/2^+$. The bound SDPF-M ^{28}Ne(J^π_f) final states up to the neutron threshold and their spectroscopic factors, from the $\langle {}^{28}{\rm Ne}(J^\pi_f)|\,{}^{29}{\rm Ne}(J^\pi)\rangle$ single-particle overlaps, are listed in Tables VI ($3/2^+$ and $3/2^-$ ^{29}Ne cases) and VII ($7/2^-$ and $1/2^+$ ^{29}Ne cases). The tables list both the $\sigma^{\rm th}_{-1n}(\alpha)$ and the $\sigma_{\rm sp}(\alpha)$ of Eq. (3) for each contributing transition. To aid comparison, this extensive set of results is summarized in Table II, which lists the cross sections to the ^{28}Ne ground state, the summed cross sections to all bound excited states, and the fractional (percentage) contribution of the ground-state transition. The corresponding experimental values are also listed. We can conclude that, for the C target data, only the

TABLE III. Summary of the calculated $1n$-removal cross sections of ^{29}Ne on C ($\sigma^{\rm th}_{-1n}$) for the different assumed spin parities of ^{29}Ne$_{\rm g.s.}$, taken from Tables VI and VII. Cross sections and percentage contributions (to the inclusive cross section to all bound states of ^{28}Ne) arising from low-ℓ ($s_{1/2}$ and $p_{3/2}$) and high-ℓ ($d_{3/2}$, $d_{5/2}$, and $f_{7/2}$) neutron removal are listed.

	^{29}Ne: J^π			
	$3/2^+$	$3/2^-$	$7/2^-$	$1/2^+$
$\sigma^{\rm th}_{-1n}$ (mb)				
s	5.35	1.17	0.76	6.07
p	10.92	43.36	6.67	15.63
d	21.36	5.38	15.30	18.26
f	25.4 4	19.10	25.38	15.16
$s+p$:$d+f$	26%:74%	65%:35%	15%:85%	39%:61%

TABLE IV. Summary of the calculated Coulomb dissociation cross sections of ^{29}Ne on Pb [$\sigma_{-1n}(E1)$] for the different assumed spin parities of ^{29}Ne. Calculations include all ^{28}Ne final states in Tables VI and VII with the SM spectroscopic factors listed there. The ^{28}Ne(0^+) ground-state (g.s.) cross section, the sum of the cross sections for all ^{28}Ne* excited states, and their sum, the inclusive cross section for all ^{28}Ne bound SM final states, are listed. Calculations were carried out to an upper limit on the continuum energy integrals of 10 MeV. In each case, the calculated percentage contribution of the g.s. transition to the inclusive cross section is listed. The experimental (expt.) results in Table I are also listed.

	^{29}Ne: J^π				
	$3/2^+$	$3/2^-$	$7/2^-$	$1/2^+$	Expt.
$\sigma_{-1n}(E1)$ (mb)					
^{28}Ne(0^+_1)	48.0	169.6	29.1	19.0	176(50)
^{28}Ne*	92.4	67.0	58.3	107.1	46(49)
Inclusive	140.3	236.6	87.4	126.0	222(36)
g.s. fraction	34%	72%	33%	15%	79(26)%

$3/2^-$, SDPF-M ^{29}Ne ground-state wave function is consistent with the measured cross sections, in particular, with regard to the absolute and fractional strength of the ground state–to–ground state transition, but also with regard to the absolute inclusive cross section.

2. *Theoretical analysis of the* ^{28}Ne *momentum distribution*

The calculated momentum distributions of the ^{28}Ne reaction residues, for the different assumed spin parities of ^{29}Ne$_{g.s.}$, and the partial cross sections and ^{28}Ne final-state energies from Tables VI and VII are shown in Fig. 5. The momentum distribution calculations use the same neutron bound-state and neutron- and ^{28}Ne-carbon optical potentials (S-matrix) information as used in the cross-section calculations.

For each assumed spin parity of the ^{29}Ne(J^π) ground state, the sums of contributions to the momentum distributions from neutron removals with ℓ_j values $s_{1/2}$, $p_{3/2}$, $d_{3/2}$ (plus $d_{5/2}$), and $f_{7/2}$, as summarized in Table III, and the final-state-inclusive momentum distributions, their sum, are shown. We note that only the calculations for the ^{29}Ne($3/2^-$) wave function reproduce the magnitude and the width of the measured inclusive momentum distribution. As mentioned in Sec. III B, the width of the measured ^{28}Ne inclusive momentum distribution is narrow, 98(12) MeV/c (FWHM). We note that the calculations indicate that this narrow width is primarily a result of the significant p-wave component, as shown in Fig. 5(b).

TABLE V. Deduced Coulomb dissociation cross sections of ^{29}Ne on Pb [$\sigma_{-1n}(E1)$] when using the constant, geometrical $\Gamma = 2.13(45)$ value (as used in Table I) and when using the Γ_{th} values from the eikonal model nuclear cross-section calculations (see text). The theoretical (theor.) cross sections, from Table IV, for the $3/2^-$ SM wave function are listed for comparison.

	Theor. $3/2^-$	Expt. Γ_{th}	Expt. Γ
$\sigma_{-1n}(E1)$ (mb)			
^{28}Ne(0^+_1)	169.6	153(50)	176(50)
^{28}Ne*	67.0	54(45)	46(49)
Inclusive	236.6	208(15)	222(36)
Ground-state fraction	72%	74(25)%	79(26)%

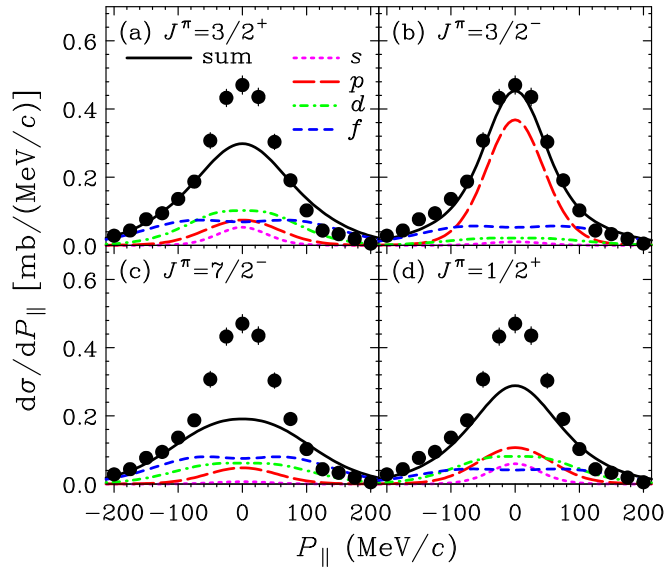

FIG. 5. Measured inclusive momentum distribution of ^{28}Ne residues after reactions on the carbon target are compared with absolute theoretical calculations based on the ^{29}Ne(J^π) SM states with (a) $J^\pi = 3/2^+$, (b) $J^\pi = 3/2^-$, (c) $J^\pi = 7/2^-$, and (d) $J^\pi = 1/2^+$. The summed contributions to the calculated inclusive momentum distributions from neutron removal (overlap) components with each ℓ value are also shown (see legend).

To understand the widths generated by the different ^{29}Ne(J^π) SM wave functions and overlaps we note that the minimum FWHM intrinsic widths of the distributions for removal of a neutron with $\ell = 0$, 1, 2, and 3 (i.e., those calculated using the ground state–to–ground state separation energy of 0.96 MeV) are 51.5, 84.8, 175.2, and 281.7 MeV/c, respectively. The agreement of the observed FWHM width of 98(12) MeV/c with the wave function with a dominant p-wave component is thus clear.

In contrast to the $3/2^-$ case, the $3/2^+$, $7/2^-$, and $1/2^+$ calculations are dominated by $\ell = 2$ and 3 contributions, resulting in momentum distributions wider than that measured, as shown in Figs. 5(a), 5(c), and 5(d).

C. Lead target analysis

1. *Cross sections*

For the Pb target, similarly to the C target case, Coulomb breakup cross sections have been calculated assuming the ^{29}Ne(J^π) ground state to be described by the lowest-lying SDPF-M SM wave functions, with spin parities $3/2^+$, $3/2^-$, $7/2^-$, and $1/2^+$. Calculations for each bound ^{28}Ne(J^π_f) final state (in Tables VI and VII) were performed using the virtual photon spectrum approach [39]. These $E1$ dissociation cross sections, which involve an integral over energy of the product of the ^{29}Ne* $dB(E1)/dE$ distributions with the virtual photon spectrum of the heavy target, are computed to an

TABLE VI. Calculated $1n$-removal reaction partial and inclusive cross sections assuming the $3/2^+$ and $3/2^-$ SDPF-M SM states for ^{29}Ne. The $1n$-removal partial cross sections to all bound ^{28}Ne SM final states below the neutron threshold of 4.18 MeV are listed. The final theoretical cross sections, $\sigma^{\rm th}_{-1n}$, include the center-of-mass correction factor $[A/(A-1)]^{N_{\rm osc}}$ to the SM spectroscopic factors. Errors in the ratio of cross sections, $R_s = \sigma^{\rm exp}_{-1n}/\sigma^{\rm th}_{-1n}$, reflect only the errors quoted in the measurements.

Reaction	E_x (MeV)	J^π_f	$n\ell_j$	$\sigma_{\rm sp}$ (mb)	C^2S	$\sigma^{\rm th}_{-1n}$(C) (mb)	$\sigma^{\rm exp}_{-1n}$(C) (mb)	R_s
C[^{29}Ne($3/2^+$), ^{28}Ne($J_f{}^\pi$)]	0.00	0^+_1	$1d_{3/2}$	29.47	0.419	13.25	36(7)	
$S_n(^{29}\text{Ne}) = 0.96$ MeV	1.36	2^+_1	$2s_{1/2}$	45.28	0.080	3.89		
			$1d_{3/2}$	22.67	0.138	3.36		
			$1d_{5/2}$	25.72	0.006	0.17		
	2.21	0^+_2	$1d_{3/2}$	20.19	0.139	3.01		
	2.76	4^+_1	$1d_{5/2}$	21.51	0.006	0.14		
	2.99	2^+_2	$2s_{1/2}$	32.90	0.039	1.38		
			$1d_{3/2}$	18.48	0.060	1.19		
			$1d_{5/2}$	20.98	0.002	0.05		
	3.57	2^-_1	$2p_{3/2}$	32.80	0.045	1.64		
		2^-_1	$1f_{7/2}$	18.91	0.402	8.45		
	3.69	3^-_1	$2p_{3/2}$	32.36	0.258	9.28		
		3^-_1	$1f_{7/2}$	18.77	0.233	4.86		
	3.90	5^-_1	$1f_{7/2}$	18.52	0.590	12.14		
	3.98	2^+_3	$2s_{1/2}$	28.59	0.003	0.09		
			$1d_{5/2}$	19.07	0.009	0.18		
	3.99	4^+_2	$1d_{5/2}$	19.05	0.001	0.02		
		Inclusive				63.07	74(2)	1.17(3)
C[^{29}Ne($3/2^-$), ^{28}Ne($J_f{}^\pi$)]	0.00	0^+_1	$2p_{3/2}$	64.93	0.438	31.60	36(7)	
$S_n(^{29}\text{Ne}) = 0.96$ MeV	1.36	2^+_1	$2p_{3/2}$	45.45	0.072	3.64		
			$1f_{7/2}$	22.33	0.167	4.14		
	2.21	0^+_2	$2p_{3/2}$	39.26	0.005	0.22		
	2.76	4^+_1	$1f_{7/2}$	19.97	0.417	9.25		
	2.99	2^+_2	$2p_{3/2}$	35.19	0.066	2.58		
			$1f_{7/2}$	19.65	0.015	0.33		
	3.57	2^-_1	$2s_{1/2}$	30.20	0.036	1.17		
			$1d_{3/2}$	17.45	0.035	0.66		
	3.69	3^-_1	$1d_{3/2}$	17.25	0.236	4.37		
			$1d_{5/2}$	19.58	0.017	0.36		
	3.98	2^+_3	$2p_{3/2}$	31.35	0.153	5.33		
			$1f_{7/2}$	18.43	0.005	0.10		
	3.99	4^+_2	$1f_{7/2}$	18.42	0.258	5.28		
		Inclusive				69.01	74(2)	1.07(3)

upper energy limit $E_{\rm max}$. The $dB(E1)/dE$ distributions are calculated using the same n-^{28}Ne potentials and geometries as used for the C target analysis. The Coulomb breakup integrals, over the dissociated n-^{28}Ne(J^π_f) relative energies, are found to be reasonably converged when $E_{\rm max}$ is chosen to include breakup configurations up to 10 MeV above the ^{29}Ne breakup threshold. That is, $E_{\rm max} = S^*_n + 10$ MeV, where S^*_n is the neutron separation energy from the ^{29}Ne ground state to the ^{28}Ne final state of interest.

The results of these calculations are summarized in Table IV, which, like Table II, lists the cross sections for the ^{28}Ne ground state, the summed cross sections for all bound excited states, and the fractional (percentage) contribution of the ground-state transition. The corresponding experimental values from Table I are also listed. The dominant contributions to these $E1$ cross sections, and the $dB(E1)/dE$ strength, arise from breakup energies $E_{\rm max} \leqslant S^*_n + 6$ MeV, with smaller higher-energy contributions from transitions to the more excited final states and/or involving orbitals with larger ℓ. For example, if restricted to $E_{\rm max} = S^*_n + 6$ MeV, the inclusive cross sections (% ground-state contribution) are 103.3 mb (37%), 211.5 mb (78%), 56.5 mb (26%), and 98.8 mb (19%) for the $3/2^+$, $3/2^-$, $7/2^-$, and $1/2^+$ states, respectively, consistent with Table IV. The results show that, as for the C target data, only the calculations based on the $3/2^-$, SDPF-M ^{29}Ne ground-state wave function are consistent with the measured cross sections. Specifically, the absolute and fractional strengths of the ground state–to–ground state transition and the absolute inclusive $E1$ cross section are consistent only with the ^{29}Ne($3/2^-$) wave function.

2. Γ *factor analysis*

In Sec. IV C 1 the calculated Coulomb dissociation cross sections for the Pb target were compared with experimental values deduced using the often-used, geometrical Γ factor of

TABLE VII. Calculated $1n$-removal reaction partial and inclusive cross sections assuming the $7/2^-$ and $1/2^+$ SDPF-M SM states for ^{29}Ne. The $1n$-removal partial cross sections for all bound ^{28}Ne SM final states below the neutron threshold of 4.18 MeV are listed. The final theoretical cross sections, $\sigma^{\rm th}_{-1n}$, include the center-of-mass correction factor $[A/(A-1)]^{N_{\rm osc}}$ to the SM spectroscopic factors. Errors in the ratio of cross sections, $R_s = \sigma^{\rm exp}_{-1n}/\sigma^{\rm th}_{-1n}$, reflect only the errors quoted in the measurements.

Reaction	E_x (MeV)	J^π_f	$n\ell_j$	$\sigma_{\rm sp}$ (mb)	C^2S	$\sigma^{\rm th}_{-1n}$(C) (mb)	$\sigma^{\rm exp}_{-1n}$(C) (mb)	R_s
C[^{29}Ne($7/2^-$), ^{28}Ne(J^π_f)]	0.00	0^+_1	$1f_{7/2}$	25.78	0.554	15.87	36(7)	
$S_n(^{29}\text{Ne}) = 0.96$ MeV	1.36	2^+_1	$2p_{3/2}$	45.45	0.033	1.67		
			$1f_{7/2}$	22.33	0.017	0.42		
	2.21	0^+_2	$1f_{7/2}$	20.80	0.052	1.20		
	2.76	4^+_1	$2p_{3/2}$	36.27	0.039	1.57		
			$1f_{7/2}$	19.97	0.061	1.35		
	2.99	2^+_2	$2p_{3/2}$	35.19	0.046	1.80		
			$1f_{7/2}$	19.65	0.059	1.29		
	3.57	2^-_1	$1d_{3/2}$	17.45	0.229	4.29		
			$1d_{5/2}$	19.80	0.005	0.11		
	3.69	3^-_1	$2s_{1/2}$	29.70	0.024	0.76		
			$1d_{3/2}$	17.25	0.151	2.79		
	3.90	5^-_1	$1d_{3/2}$	16.92	0.447	8.12		
	3.98	2^+_3	$1f_{7/2}$	18.43	0.150	3.07		
	3.99	4^+_2	$2p_{3/2}$	31.32	0.047	1.64		
			$1f_{7/2}$	18.42	0.106	2.17		
		Inclusive				48.11	74(2)	1.54(4)
C[^{29}Ne($1/2^+$), ^{28}Ne(J^π_f)]	0.00	0^+_1	$2s_{1/2}$	72.27	0.035	2.71	36(7)	
$S_n(^{29}\text{Ne}) = 0.96$ MeV	1.36	2^+_1	$1d_{3/2}$	22.67	0.642	15.61		
			$1d_{5/2}$	25.72	0.002	0.06		
	2.21	0^+_2	$2s_{1/2}$	37.66	0.083	3.35		
	2.99	2^+_2	$1d_{3/2}$	18.48	0.131	2.60		
	3.57	2^-_1	$2p_{3/2}$	32.80	0.429	15.63		
	3.69	3^-_1	$1f_{7/2}$	18.77	0.727	15.16		
		Inclusive				55.13	74(2)	1.32(4)

2.13(45) in Eq. (1). As stated earlier, a significant uncertainty is already included in this value. Recently, and with particular relevance to weakly bound projectiles, Yoshida *et al.* [40] showed, based on model calculations, that Γ values deduced from theoretical cross sections have a residual dependence on the separation energy and the orbital angular momentum of the removed neutron.

To estimate the significance of such an uncertainty in the nuclear contribution to the lead target cross section in the present work, we use the eikonal model, as discussed for the C target calculations in Sec. IV B 1, to calculate the nuclear breakup contributions for Pb. Hence, we compute theoretical $\Gamma_{\rm th}$ values for each of the transitions in Tables VI and VII. We define $\Gamma_{\rm th}(\alpha) = \sigma^{\rm th}_{-1n}(\alpha,\text{Pb})/\sigma^{\rm th}_{-1n}(\alpha,\text{C})$. The nuclear $1n$-removal calculations for Pb include the Coulomb interaction only through the introduction of the small Coulomb deflection correction to the center-of-mass impact parameter of the projectile, b_p, with wave-number k_p and Sommerfeld parameter η. That is, in the eikonal model integral over all impact parameters of the projectile, we make the replacement

$$k_p b_p \rightarrow \left[\eta + \sqrt{\eta^2 + k_p^2 b_p^2}\right],$$

which introduces small shifts to the values of the impact parameters at which the residue- and the neutron-target S-matrices are computed.

We quantify the expected (in)sensitivity of the Pb target data analysis to using, instead, these $\Gamma_{\rm th}$. We summarize the results of this analysis only for the ^{29}Ne($3/2^-$) case, since the other SM J^π possibilities are now excluded by the cross-section and momentum distribution data on the carbon target, as well as the Coulomb dissociation calculations listed in Table IV. For the $3/2^-$ case, the computed $\Gamma_{\rm th}$ for the ground-state transition is $\Gamma_{\rm th}[^{28}\text{Ne}(0^+)] = 2.77$, while the partial cross-section-weighted average of the $\Gamma_{\rm th}(\alpha)$ for all bound excited states (with their higher effective separation energies) is $\Gamma_{\rm th}(^{28}\text{Ne}^*) = 1.90$. In Table V we compare the re-evaluated empirical $\sigma_{-1n}(E1)$ when using the theoretical $\Gamma_{\rm th}$ ("Expt. $\Gamma_{\rm th}$") with the earlier cross sections from Table I ("Expt. Γ"), together with the theoretical $E1$ cross sections for ^{29}Ne($3/2^-$) from Table IV. We can conclude that changes in the nuclear contribution to the Pb target cross-section data caused by variations of the value of Γ within theoretical expectations do not affect the conclusions of this work regarding the ^{29}Ne($3/2^-$) spin and parity assignment.

D. Spectroscopic factors

Tables II and IV show that the data on the C and Pb targets are consistent with calculations of the nuclear and Coulomb neutron-removal mechanisms, assuming the ^{29}Ne($3/2^-$) SDPF-M ground-state wave function. Since, for

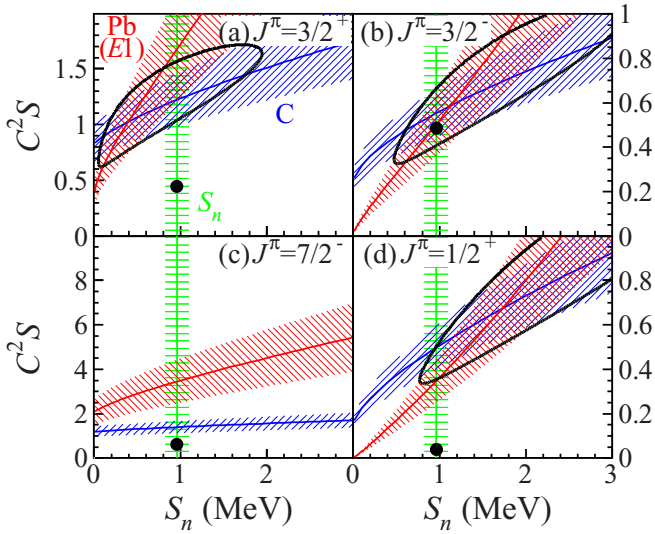

FIG. 6. C^2S deduced from the ratios of the measured and calculated ^{28}Ne ground-state partial cross sections on the C target (blue hatched areas) and Coulomb breakup (red hatched areas) on the Pb target as a function of the assumed S_n and J^π of ^{29}Ne. The green hatched area shows the value and 1σ error on the empirical S_n. Calculations are shown for (a) $3/2^+$, $^{28}\mathrm{Ne}(0^+_1)\otimes 1d_{3/2}$; (b) $3/2^-$, $^{28}\mathrm{Ne}(0^+_1)\otimes 2p_{3/2}$; (c) $7/2^-$, $^{28}\mathrm{Ne}(0^+_1)\otimes 1f_{7/2}$; and (d) $1/2^+$, $^{28}\mathrm{Ne}(0^+_1)\otimes 2s_{1/2}$ ^{29}Ne ground-state configurations. The filled black circle in each panel shows the theoretical ^{29}Ne ground state–to–^{28}Ne ground state SM spectroscopic factor, $[A/(A-1)]^{N_{\rm osc}}C^2S$, for each J^π.

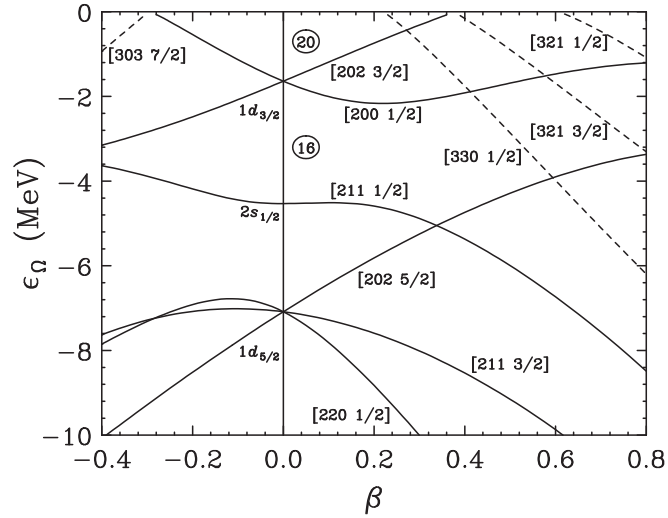

FIG. 7. Neutron single-particle levels in a deformed Woods-Saxon well as a function of the quadrupole deformation parameter β. The depth, diffuseness, and radius of the potential (for $A = 28$) are -41.0 MeV, 0.67 fm, and 3.856 fm, respectively. Positive- and negative-parity levels are plotted as solid and dashed curves, respectively. The asymptotic quantum numbers $[Nn_z\lambda\Omega]$ are also shown.

^{29}Ne, S_n is rather well determined [29], we can also extract empirical values for the ground-state C^2S based on the single-particle cross sections of the model calculations on the C and Pb targets.

Figure 6 shows, as a function of the assumed S_n and J^π of ^{29}Ne, the two independent C^2S values, and their uncertainties, deduced from the ground-state cross-section ratios, $\sigma_{-1n}(\mathrm{C};0^+_1)/\sigma_{\rm sp}(\mathrm{C};n\ell j)$ and $\sigma_{-1n}(E1;0^+_1)/\sigma_{\rm sp}(E1;n\ell j)$, for the two targets. The blue (red) hatched regions show these C^2S for the C target (Pb target, Coulomb breakup) data analysis. The $\sigma_{-1n}(\mathrm{C};0^+_1)$ and $\sigma_{-1n}(E1;0^+_1)$ values used are those from Table I. In addition, the green hatched area shows the value and 1σ error of the empirical S_n. So the C^2S may be evaluated by the overlap of these three hatched areas, which can then be compared with the SM C^2S value. The solid lines in Figs. 6(a), 6(b), and 6(d) show the 1σ limit (68% confidence level) on the overlap of the deduced C^2S from these two cross-section ratios only. The filled black circle in each panel shows the theoretical $^{29}\mathrm{Ne}(J^\pi)$-to-^{28}Ne ground-state spectroscopic factor, $[A/(A-1)]^{N_{\rm osc}}C^2S$, from the SM calculation. We see that only the $^{29}\mathrm{Ne}(J^\pi = 3/2^-)$ ground-state spin-parity assignment is consistent with the measured data sets, S_n, and the SDPF-M large-scale SM calculations.

From Fig. 6(b) we deduce an empirical $3/2^-$ ground-state spectroscopic factor of $C^2S(0^+_1;2p_{3/2}) = 0.54(9)$. If, instead, we take the Coulomb dissociation cross sections as deduced from the theoretical $\Gamma_{\rm th}$ ("Expt. $\Gamma_{\rm th}$" in Table V), then the extracted spectroscopic factor is $C^2S(0^+_1;2p_{3/2}) = 0.51(9)$, to be compared with the effective SM spectroscopic factor, $(29/28)^3C^2S(\mathrm{SDPF{-}M}) = 0.49$.

V. DISCUSSION

A parity inversion is now known to take place between the ground state of $^{27}\mathrm{Ne}(3/2^+)$ and that of $^{31}\mathrm{Ne}(3/2^-)$, spanning the edge of the island of inversion at $Z = 10$. This level inversion is reproduced by large-scale SM calculations and the SDPF-M effective interaction. In ^{29}Ne, the lowest $3/2^+$ and $3/2^-$ SM configurations are separated by only 73 keV. The present work shows that a $3/2^-$ ^{29}Ne ground-state spin assignment is consistent with the measured data sets, the known S_n, and the SDPF-M large-scale SM calculations and that the parity inversion actually occurs upon going between ^{27}Ne and ^{29}Ne. In particular, the importance of the p-wave neutron contribution to the $\langle\, ^{28}\mathrm{Ne}(0^+_1)|^{29}\mathrm{Ne}_{\rm g.s.}(J^\pi)\rangle$ overlap in reproducing the measured data is indicative of the breakdown of conventional shell ordering (of the naive spherical SM) and of the presence of deformation in ^{29}Ne.

The dominant SM configuration and deformation of ^{29}Ne can be understood by reference to the Nilsson diagram in Fig. 7. The $3/2^-_1$ SM state is composed of $1\hbar\omega$ (32.4%), $3\hbar\omega$ (66.6%), and $5\hbar\omega$ (1.0%) configurations. The dominant $3\hbar\omega$ configuration refers to a $3p$-$4h$ configuration in ^{29}Ne, where np-mh stands for n fp-shell particles and m sd-shell hole components $[\nu(sd)^{-4}(fp)^3]$. In terms of the Nilsson diagram, this configuration corresponds to the [3213/2] orbital at large quadrupole deformations, $0.58 < \beta < 0.80$. This state is also mixed with $1p-2h$ $[\nu(sd)^{-2}(fp)^1]$ configurations, specifically, with the moderately deformed [3301/2] configuration with $0.27 < \beta < 0.41$. Regardless of the details of such

configuration mixing, these large deformations are consistent with ^{29}Ne lying within the island of inversion. We note also that neutron removal from the $3\hbar\omega$ (66.6%), $J^\pi = 3/2^-$ configuration is expected to overlap strongly with, and is consistent with, the dominant ($\approx$62%) $2\hbar\omega$ ^{28}Ne ground-state component (Fig. 3). In both the shell and the Nilsson models, the mechanism driving deformation in ^{29}Ne can be linked to the Jahn-Teller effect, whereby the near-degeneracy of the $\nu 1f_{7/2}$ and $\nu 2p_{3/2}$ orbitals results in the disappearance of magicity at $N = 28$, as discussed in Refs. [5–7,10,11,13]. The results measured here support the view that the fp-shell degeneracy, and associated Jahn-Teller effect, plays a significant role throughout the island of inversion.

VI. CONCLUSIONS

Measurements of the cross sections for $1n$ removal from the neutron-rich nucleus ^{29}Ne on carbon and lead targets and the parallel momentum distribution of the ^{28}Ne residues from the carbon target, at around 240 MeV/nucleon, have been presented. The nucleus ^{29}Ne is important for understanding the extent of the island of inversion, as a parity inversion is known to take place between the ground state of ^{27}Ne($3/2^+$) and that of ^{31}Ne($3/2^-$). This inversion is reproduced by large-scale SM calculations using the SDPF-M effective interaction, whereas, in ^{29}Ne, the $3/2^+$ and $3/2^-$ SM levels are separated by only 73 keV.

The width of the measured inclusive parallel momentum distribution was found to be narrow [98(12) MeV/c (FWHM)], suggestive of the dominance of low-ℓ valence neutron configurations in ^{29}Ne. A detailed comparison has been carried out of the inclusive and partial neutron-removal cross sections and the ^{28}Ne parallel momentum distribution on the carbon target with reaction calculations combined with SM spectroscopic information. As such, a $3/2^-$ spin-parity assignment has been made for the ^{29}Ne ground state. This indicates that ^{29}Ne lies within the ($N \approx 20$) island of inversion and is dominated by a ^{28}Ne(0_1^+) $\otimes$ $2p_{3/2}$ neutron configuration. Taken together with the enhanced total interaction cross section of ^{29}Ne with respect to ^{28}Ne [12] and the moderate single-neutron binding, ^{29}Ne may exhibit a somewhat extended halo-like valence neutron spatial distribution. The systematics of the present and earlier data on the neutron-rich Ne isotopes strongly suggest that the degeneracy of the fp shells and the Jahn-Teller effect play a crucial role in the formation of the island of inversion.

ACKNOWLEDGMENTS

We thank the RIKEN accelerator staff for the excellent beam delivery. The RIBF is operated by the RIKEN Nishina Center and the Center for Nuclear Study (CNS), University of Tokyo. We are grateful to Y. Utsuno and T. Otsuka for the theoretical assistance with shell-model calculations. Fruitful discussions with I. Hamamoto are acknowledged. The present work was supported in part by JSPS KAKENHI Grant No. 22340053, MEXT KAKENHI Grant No. 24105005, and NRF Grant No. R32-2008-000-10155-0 (WCU) from MEST Korea. N.K. acknowledges the Grant-in-Aid for JSPS Fellows (No. 25 · 10601) from MEXT. J.A.T. acknowledges support from Science and Technology Facilities Council (UK) Grant Nos. ST/J000051 and ST/L005743. R.K. acknowledges support from NSERC. N.A.O. acknowledges partial support from the Franco-Japanese LIA-International Associated Laboratory for Nuclear Structure Problems.

[1] T. Otsuka, Phys. Scr. T **152**, 014007 (2013), and references therein.
[2] O. Sorlin and M.-G. Porquet, Prog. Part. Nucl. Phys. **61**, 602 (2008), and references therein.
[3] E. Caurier, F. Nowacki, and A. Poves, Phys. Rev. C **90**, 014302 (2014), and references therein.
[4] E. K. Warburton, J. A. Becker, and B. A. Brown, Phys. Rev. C **41**, 1147 (1990).
[5] I. Hamamoto, Phys. Rev. C **76**, 054319 (2007).
[6] I. Hamamoto, Phys. Rev. C **81**, 021304(R) (2010).
[7] I. Hamamoto, Phys. Rev. C **85**, 064329 (2012).
[8] H. A. Jahn and E. Teller, Proc. R. Soc. A **161**, 220 (1937).
[9] P.-G. Reinhard and E. W. Otten, Nucl. Phys. A **420**, 173 (1984).
[10] T. Nakamura, N. Kobayashi, Y. Kondo, Y. Satou, N. Aoi, H. Baba, S. Deguchi, N. Fukuda, J. Gibelin, N. Inabe, M. Ishihara, D. Kameda, Y. Kawada, T. Kubo, K. Kusaka, A. Mengoni, T. Motobayashi, T. Ohnishi, M. Ohtake, N. A. Orr, H. Otsu, T. Otsuka, A. Saito, H. Sakurai, S. Shimoura, T. Sumikama, H. Takeda, E. Takeshita, M. Takechi, S. Takeuchi, K. Tanaka, K. N. Tanaka, N. Tanaka, Y. Togano, Y. Utsuno, K. Yoneda, A. Yoshida, and K. Yoshida, Phys. Rev. Lett. **103**, 262501 (2009).
[11] T. Nakamura, N. Kobayashi, Y. Kondo, Y. Satou, J. A. Tostevin, Y. Utsuno, N. Aoi, H. Baba, N. Fukuda, J. Gibelin, N. Inabe, M. Ishihara, D. Kameda, T. Kubo, T. Motobayashi, T. Ohnishi, N. A. Orr, H. Otsu, T. Otsuka, H. Sakurai, T. Sumikama, H. Takeda, E. Takeshita, M. Takechi, S. Takeuchi, Y. Togano, and K. Yoneda, Phys. Rev. Lett. **112**, 142501 (2014).
[12] M. Takechi *et al.*, Phys. Lett. B **707**, 357 (2012).
[13] N. Kobayashi,T. Nakamura, Y. Kondo, J. A. Tostevin, Y. Utsuno, N. Aoi, H. Baba, R. Barthelemy, M. A. Famiano, N. Fukuda, N. Inabe, M. Ishihara, R. Kanungo, S. Kim, T. Kubo, G. S. Lee, H. S. Lee, M. Matsushita, T. Motobayashi, T. Ohnishi, N. A. Orr, H. Otsu, T. Otsuka, T. Sako, H. Sakurai, Y. Satou, T. Sumikama, H. Takeda, S. Takeuchi, R. Tanaka, Y. Togano, and K. Yoneda, Phys. Rev. Lett. **112**, 242501 (2014).
[14] M. Takechi *et al.*, Phys. Rev. C **90**, 061305(R) (2014).
[15] Y. Utsuno, T. Otsuka, T. Mizusaki, and M. Honma, Phys. Rev. C **60**, 054315 (1999).
[16] L. Gaudefroy, W. Mittig, N. A. Orr, S. Varet, M. Chartier, P. Roussel-Chomaz, J. P. Ebran, B. Fernandez-Dominguez, G. Fremont, P. Gangnant, A. Gillibert, S. Grevy, J. F. Libin, V. A. Maslov, S. Paschalis, B. Pietras, Y. E. Penionzhkevich, C. Spitaels, and A. C. C. Villari, Phys. Rev. Lett. **109**, 202503 (2012).

[17] W. N. Catford, C. N. Timis, R. C. Lemmon, M. Labiche, N. A. Orr, B. Fernandez-Dominguez, R. Chapman, M. Freer, M. Chartier, H. Savajols, M. Rejmund, N. L. Achouri, N. Amzal, N. I. Ashwood, T. D. Baldwin, M. Burns, L. Caballero, J. M. Casadjian, N. Curtis, G. deFrance, W. Gelletly, X. Liang, S. D. Pain, V. P. E. Pucknell, B. Rubio, O. Sorlin, K. Spohr, C. Theisen, and D. D. Warner, Phys. Rev. Lett. **104**, 192501 (2010).
[18] J. R. Terry *et al.*, Phys. Lett. B **640**, 86 (2006).
[19] Z. Dombrádi, Z. Elekes, A. Saito, N. Aoi, H. Baba, K. Demichi, Z. Fulop, J. Gibelin, T. Gomi, H. Hasegawa, N. Imai, M. Ishihara, H. Iwasaki, S. Kanno, S. Kawai, T. Kishida, T. Kubo, K. Kurita, Y. Matsuyama, S. Michimasa, T. Minemura, T. Motobayashi, M. Notani, T. Ohnishi, H. J. Ong, S. Ota, A. Ozawa, H. K. Sakai, H. Sakurai, S. Shimoura, E. Takeshita, S. Takeuchi, M. Tamaki, Y. Togano, K. Yamada, Y. Yanagisawa, and K. Yoneda, Phys. Rev. Lett. **96**, 182501 (2006).
[20] A. Obertelli *et al.*, Phys. Lett. B **633**, 33 (2006).
[21] S. M. Brown, W. N. Catford, J. S. Thomas, B. Fernandez-Dominguez, N. A. Orr, M. Labiche, M. Rejmund, N. L. Achouri, H. Al Falou, N. I. Ashwood, D. Beaumel, Y. Blumenfeld, B. A. Brown, R. Chapman, M. Chartier, N. Curtis, G. de France, N. de Sereville, F. Delaunay, A. Drouart, C. Force, S. Franchoo, J. Guillot, P. Haigh, F. Hammache, V. Lapoux, R. C. Lemmon, A. Leprince, F. Marechal, X. Mougeot, B. Mouginot, L. Nalpas, A. Navin, N. P. Patterson, B. Pietras, E. C. Pollacco, A. Ramus, J. A. Scarpaci, I. Stefan, and G. L. Wilson, Phys. Rev. C **85**, 011302(R) (2012).
[22] H. Liu *et al.*, JPS Conf. Proc. **6**, 030003 (2015).
[23] V. Tripathi, S. L. Tabor, C. R. Hoffman, M. Wiedeking, A. Volya, P. F. Mantica, A. D. Davies, S. N. Liddick, W. F. Mueller, A. Stolz, B. E. Tomlin, T. Otsuka, and Y. Utsuno, Phys. Rev. C **73**, 054303 (2006).
[24] N. A. Orr *et al.*, Phys. Lett. B **258**, 29 (1991).
[25] X. G. Zhou *et al.*, Phys. Lett. B **260**, 285 (1991).
[26] P. G. Hansen and J. A. Tostevin, Annu. Rev. Nucl. Part. Sci. **53**, 219 (2003), and references therein.
[27] N. Kobayashi, T. Nakamura, J. A. Tostevin, Y. Kondo, N. Aoi, H. Baba, S. Deguchi, J. Gibelin, M. Ishihara, Y. Kawada, T. Kubo, T. Motobayashi, T. Ohnishi, N. A. Orr, H. Otsu, H. Sakurai, Y. Satou, E. C. Simpson, T. Sumikama, H. Takeda, M. Takechi, S. Takeuchi, K. N. Tanaka, N. Tanaka, Y. Togano, and K. Yoneda, Phys. Rev. C **86**, 054604 (2012).
[28] T. Aumann and T. Nakamura, Phys. Scr. T **152**, 014012 (2013).
[29] G. Audi *et al.*, Chin. Phys. C **36**, 1287 (2012); M. Wang *et al.*, **36**, 1603 (2012).
[30] B. Jurado *et al.*, Phys. Lett. B **649**, 43 (2007).
[31] Y. Yano, Nucl. Instrum. Methods Phys. Res., Sec. B **261**, 1009 (2007).
[32] T. Kubo, Nucl. Instrum. Methods Phys. Res., Sec. B **204**, 97 (2003).
[33] T. Kubo *et al.*, IEEE Trans. Appl. Supercond. **17**, 1069 (2007).
[34] S. Takeuchi *et al.*, Nucl. Instrum. Methods Phys. Res., Sec. A **763**, 596 (2014).
[35] M. Belleguic, F. Azaiez, Z. Dombradi, M. J. Lopez-Jimenez, T. Otsuka, M. G. Saint-Laurent, D. Sohler, O. Sorlin, M. Stanoiu, Y. Utsuno, Y. E. Penionzhkevich, N. L. Achouri, J. C. Angelique, C. Borcea, C. Bourgeois, J. M. Daugas, F. De Oliveira-Santos, Z. Dlouhy, C. Donzaud, J. Duprat, Z. Elekes, S. Grevy, D. Guillemaud-Mueller, S. Leenhardt, M. Lewitowicz, S. M. Lukyanov, W. Mittig, M. G. Porquet, F. Pougheon, P. Roussel-Chomaz, H. Savajols, Y. Sobolev, C. Stodel, and J. Timar, Phys. Rev. C **72**, 054316 (2005).
[36] J. A. Tostevin, Nucl. Phys. A **682**, 320 (2001).
[37] P. Doornenbal *et al.*, Phys. Rev. Lett. **103**, 032501 (2009).
[38] A. E. L. Dieperink and T. L. de Forest Jr., Phys. Rev. C **10**, 543 (1974).
[39] C. A. Bertulani and G. Baur, Phys. Rep. **163**, 299 (1988).
[40] K. Yoshida, T. Fukui, K. Minomo, and K. Ogata, Prog. Theor. Exp. Phys. **2014**, 053D03 (2014).
[41] A. Gade, P. Adrich, D. Bazin, M. D. Bowen, B. A. Brown, C. M. Campbell, J. M. Cook, T. Glasmacher, P. G. Hansen, K. Hosier, S. McDaniel, D. McGlinchery, A. Obertelli, K. Siwek, L. A. Riley, J. A. Tostevin, and D. Weisshaar, Phys. Rev. C **77**, 044306 (2008).